PHYSICAL REVIEW B **95**, 094406 (2017)

Cluster multipole theory for anomalous Hall effect in antiferromagnets

M.-T. Suzuki,[1] T. Koretsune,[1,2] M. Ochi,[3] and R. Arita[1]
[1]*RIKEN Center for Emergent Matter Science, Wako, Saitama 351-0198, Japan*
[2]*JST, PRESTO, 4-1-8 Honcho Kawaguchi, Saitama 332-0012, Japan*
[3]*Department of Physics, Osaka University, Toyonaka, Osaka 560-0043, Japan*
(Received 24 November 2016; published 7 March 2017)

We introduce a cluster extension of multipole moments to discuss the anomalous Hall effect (AHE) in both ferromagnetic (FM) and antiferromagnetic (AFM) states in a unified framework. We first derive general symmetry requirements for the AHE in the presence or absence of the spin-orbit coupling by considering the symmetry of the Berry curvature in $\boldsymbol{k}$ space. The cluster multipole (CMP) moments are then defined to quantify the macroscopic magnetization in noncollinear AFM states as a natural generalization of the magnetization in FM states. We identify the macroscopic CMP order which induces the AHE. The theoretical framework is applied to the noncollinear AFM states of Mn_3Ir, for which an AHE was predicted in a first-principles calculation, and Mn_3Z (Z = Sn, Ge), for which a large AHE was recently discovered experimentally. We further compare the AHE in Mn_3Z and bcc Fe in terms of the CMP. We show that the AHE in Mn_3Z is characterized by the magnetization of a cluster octupole moment in the same manner as that in bcc Fe characterized by the magnetization of the dipole moment.

DOI: 10.1103/PhysRevB.95.094406

I. INTRODUCTION

The modern formalism of the intrinsic anomalous Hall conductivity (AHC) provides profound insight into the anomalous Hall effect (AHE) being closely related to the topology of one-electron energy bands [1–3]. The AHE is usually observed in ferromagnetic (FM) metals, but the AHE has been studied also for certain noncollinear antiferromagnetic (AFM) states [1,4–13]. In particular, a large AHC was recently discovered for the AFM states in Mn_3Z (Z = Sn, Ge), whose magnetic geometry has no uniform magnetization [14–16]. The topological feature of these AFM states has also been investigated based on the first-principles calculations [12,13,17].

The AHE requires not only the broken time-reversal symmetry but also a certain type of magnetic structure [18,19]. Furthermore, the situation changes depending on the presence or absence of the spin-orbit (SO) coupling. For instance, the AHE requires the SO coupling in collinear FM states, characterized by uniform magnetization. The crucial role of the SO coupling for the AHE in the FM states has been discussed since its pioneering study [20]. On the other hand, in AFM systems, two types of AHE have been investigated. One is the AHE in noncoplanar spin configurations where the AHE can be induced even without the SO coupling. The AHE is characterized by the scalar spin chirality [21] and studied intensively in the context of the topological Hall effect [6,22]. The other is the AHE in coplanar spin systems such as Mn_3Sn [12,13,23]. In this case, it is not well understood whether there is a macroscopic quantity that characterizes the AHE such as the uniform magnetization or scalar spin chirality. Moreover, there is no clear explanation for what types of AFM structures induce the AHE.

The purpose of this paper is to provide comprehensive understanding of the AHE in relation to the magnetic structure. We propose an order parameter, which we call the cluster multipole (CMP) moment, to measure the symmetry breaking of commensurate noncollinear magnetic order. This systematically explains what types of AFM structures induce the AHE and whether the AHE requires the SO coupling in that AFM state.

The structure of this paper is as follows. In Sec. II, we derive a symmetry condition for finite AHC in generic noncollinear magnetic systems by considering the symmetry of the Berry curvature in $\boldsymbol{k}$ space. We show that the AHE is forbidden to emerge by some symmetry elements of the magnetic space group, whose operations preserve the magnetic structure. The derivation also leads to comprehensive understanding of the requirement of the SO coupling for the AHE. In Sec. III, we introduce CMP moments as order parameters defined for a cluster of atoms, which is a natural generalization of the local magnetic moments for atoms. The CMP characterizes the noncollinear AFM structure as analogous to the atomic magnetic multipole moments characterizing the local magnetic distribution [24–29]. We show that the AHE of Mn_3Ir and Mn_3Z is associated with the cluster octupole moments which belong to the same symmetry as the magnetic dipole moments. In Sec. IV, we calculate the electronic structure, Berry curvature, and AHC for the AFM states of Mn_3Z from first principles. As a reference, we also calculate those properties for the FM state of bcc Fe, which has been well investigated in earlier works [30–32]. We show that the AHE of the FM and AFM states can be discussed in the same framework in terms of the CMP. Finally, a summary of the results is given in Sec. V.

II. SYMMETRY ASPECT OF ANOMALOUS HALL EFFECT

A. Symmetry of the Berry curvature in k space

The intrinsic AHC is expressed as the Berry curvature integrated over the Brillouin zone (BZ) of one-electron bands below the Fermi level [33,34]:

$$\sigma_{\alpha\beta} = -\frac{e^2}{\hbar}\int \frac{d\boldsymbol{k}}{(2\pi)^3}\sum_n f[\varepsilon_n(\boldsymbol{k})-\mu]\Omega_{n,\alpha\beta}(\boldsymbol{k}), \qquad (1)$$

where n is the band index and $\alpha, \beta = x, y, z$, with $\alpha \neq \beta$. The Berry curvature for the AHC is defined as

$$\Omega_{n,\alpha\beta}(\boldsymbol{k}) = -2\mathrm{Im}\sum_{m\neq n}\frac{v_{nm,\alpha}(\boldsymbol{k})v_{mn,\beta}(\boldsymbol{k})}{[\varepsilon_m(\boldsymbol{k})-\varepsilon_n(\boldsymbol{k})]^2} \qquad (2)$$

TABLE I. Constraint on the Berry curvature in $\boldsymbol{k}$ space for some representative symmetries. Here, x, y, z express the Cartesian coordinates. $C_{n\mu}$ indicates the n-fold rotation operator along the μ axis, P is the spatial inversion operator, and T is the time-reversal operator. The mirror operation whose mirror plane is normal to the μ axis corresponds to $PC_{2\mu}$.

	Unitary operators		Antiunitary operators
C_{2z}	$\Omega^x(-k_x,-k_y,k_z) = -\Omega^x(k_x,k_y,k_z)$ $\Omega^y(-k_x,-k_y,k_z) = -\Omega^y(k_x,k_y,k_z)$ $\Omega^z(-k_x,-k_y,k_z) = \Omega^z(k_x,k_y,k_z)$	TC_{2z}	$\Omega^x(k_x,k_y,-k_z) = \Omega^x(k_x,k_y,k_z)$ $\Omega^y(k_x,k_y,-k_z) = \Omega^y(k_x,k_y,k_z)$ $\Omega^z(k_x,k_y,-k_z) = -\Omega^z(k_x,k_y,k_z)$
PC_{2z}	$\Omega^x(k_x,k_y,-k_z) = -\Omega^x(k_x,k_y,k_z)$ $\Omega^y(k_x,k_y,-k_z) = -\Omega^y(k_x,k_y,k_z)$ $\Omega^z(k_x,k_y,-k_z) = \Omega^z(k_x,k_y,k_z)$	TPC_{2z}	$\Omega^x(-k_x,-k_y,k_z) = \Omega^x(k_x,k_y,k_z)$ $\Omega^y(-k_x,-k_y,k_z) = \Omega^y(k_x,k_y,k_z)$ $\Omega^z(-k_x,-k_y,k_z) = -\Omega^z(k_x,k_y,k_z)$
$C_{2[1\bar{1}0]}$	$\Omega^x(-k_y,-k_x,-k_z) = -\Omega^y(k_x,k_y,k_z)$ $\Omega^y(-k_y,-k_x,-k_z) = -\Omega^x(k_x,k_y,k_z)$ $\Omega^z(-k_y,-k_x,-k_z) = -\Omega^z(k_x,k_y,k_z)$	$TC_{2[1\bar{1}0]}$	$\Omega^x(k_y,k_x,k_z) = \Omega^y(k_x,k_y,k_z)$ $\Omega^y(k_y,k_x,k_z) = \Omega^x(k_x,k_y,k_z)$ $\Omega^z(k_y,k_x,-k_z) = \Omega^z(k_x,k_y,k_z)$
$PC_{2[1\bar{1}0]}$	$\Omega^x(k_y,k_x,k_z) = -\Omega^y(k_x,k_y,k_z)$ $\Omega^y(k_y,k_x,k_z) = -\Omega^x(k_x,k_y,k_z)$ $\Omega^z(k_y,k_x,k_z) = -\Omega^z(k_x,k_y,k_z)$	$TPC_{2[1\bar{1}0]}$	$\Omega^x(-k_y,-k_x,-k_z) = \Omega^y(k_x,k_y,k_z)$ $\Omega^y(-k_y,-k_x,-k_z) = \Omega^x(k_x,k_y,k_z)$ $\Omega^z(-k_y,-k_x,-k_z) = \Omega^z(k_x,k_y,k_z)$
$C_{3[111]}$	$\Omega^x(k_z,k_x,k_y) = \Omega^y(k_x,k_y,k_z)$ $\Omega^y(k_z,k_x,k_y) = \Omega^z(k_x,k_y,k_z)$ $\Omega^z(k_z,k_x,k_y) = \Omega^x(k_x,k_y,k_z)$	$TC_{3[111]}$	$\Omega^x(-k_z,-k_x,-k_y) = -\Omega^y(k_x,k_y,k_z)$ $\Omega^y(-k_z,-k_x,-k_y) = -\Omega^z(k_x,k_y,k_z)$ $\Omega^z(-k_z,-k_x,-k_y) = -\Omega^x(k_x,k_y,k_z)$
$PC_{3[111]}$	$\Omega^x(-k_z,-k_x,-k_y) = \Omega^y(k_x,k_y,k_z)$ $\Omega^y(-k_z,-k_x,-k_y) = \Omega^z(k_x,k_y,k_z)$ $\Omega^z(-k_z,-k_x,-k_y) = \Omega^x(k_x,k_y,k_z)$	$TPC_{3[111]}$	$\Omega^x(k_z,k_x,k_y) = -\Omega^y(k_x,k_y,k_z)$ $\Omega^y(k_z,k_x,k_y) = -\Omega^z(k_x,k_y,k_z)$ $\Omega^z(k_z,k_x,k_y) = -\Omega^x(k_x,k_y,k_z)$

from the Kubo formula [30,35]. In these equations, $\varepsilon_n(\boldsymbol{k})$ is the eigenvalue, and

$$v_{nm,\alpha}(\boldsymbol{k}) = \frac{1}{\hbar}\left\langle u_n(\boldsymbol{k})\left|\frac{\partial \hat{H}(\boldsymbol{k})}{\partial k_\alpha}\right|u_m(\boldsymbol{k})\right\rangle, \tag{3}$$

where $u_{n\boldsymbol{k}}$ is the periodic-cell part of the Bloch states and $\hat{H}(\boldsymbol{k}) = e^{-i\boldsymbol{k}\cdot\boldsymbol{r}}\hat{H}e^{i\boldsymbol{k}\cdot\boldsymbol{r}}$. For the convenience of our discussions, we hereafter use the vector-form notations for the AHC and Berry curvature, i.e., $\boldsymbol{\sigma} = (\sigma^x,\sigma^y,\sigma^z) \equiv (\sigma_{yz},\sigma_{zx},\sigma_{xy})$ and $\Omega_n = (\Omega_n^x,\Omega_n^y,\Omega_n^z) \equiv (\Omega_{n,yz},\Omega_{n,zx},\Omega_{n,xy})$.

From Eq. (1), the appearance of the AHC σ^α is governed by the Berry curvature in $\boldsymbol{k}$ space $\Omega^\alpha(\boldsymbol{k})$. Thus, let us first discuss the symmetry of the Berry curvature in $\boldsymbol{k}$ space. The group velocity is expressed with the Berry phase correction as follows [36,37]:

$$\dot{\boldsymbol{r}} = \frac{1}{\hbar}\frac{\partial \varepsilon_n(\boldsymbol{k})}{\partial \boldsymbol{k}} - \dot{\boldsymbol{k}} \times \Omega_n(\boldsymbol{k})\,. \tag{4}$$

The transformation property of the Berry curvature with respect to the symmetry elements of magnetic space groups can be derived from this equation since the properties of $\varepsilon_n(\boldsymbol{k})$, $\dot{\boldsymbol{r}}$, $\boldsymbol{k}$, and $\dot{\boldsymbol{k}}$ are known. First, the Berry curvature is not modified by any translation operations. Second, it is transformed in the same way as ordinary vectors for rotation operations in $\boldsymbol{k}$ space. Third, the space inversion brings $\Omega_n(\boldsymbol{k})$ to $\Omega_n(-\boldsymbol{k})$. Thus, the Berry curvature $\Omega_n(\boldsymbol{k})$ behaves as an axial vector in $\boldsymbol{k}$ space. Finally, the time-reversal operation transforms $\Omega_n(\boldsymbol{k})$ to $-\Omega_n(-\boldsymbol{k})$.

These transformation properties of the Berry curvature define constraints on its structure in $\boldsymbol{k}$ space. The well-known relations are $\Omega_n(-\boldsymbol{k}) = \Omega_n(\boldsymbol{k})$ for systems with the space-inversion symmetry and $\Omega_n(-\boldsymbol{k}) = -\Omega_n(\boldsymbol{k})$ for systems with the time-reversal symmetry. Some of other relations are listed in Table I. These relations define further constraints on the Berry curvature at some $\boldsymbol{k}$ points, related to the elements of the group of $\boldsymbol{k}$. A simple example is that the Berry curvature is zero all over the BZ under both the space-inversion and time-reversal symmetries since the successive transformation of these operations results in $\Omega_n(\boldsymbol{k}) = -\Omega_n(\boldsymbol{k})$, leading to $\Omega_n(\boldsymbol{k}) = 0$. Another example is the magnetic systems which have TC_{2z} symmetry. In this case, $\Omega^z(\boldsymbol{k}) = 0$ on the $k_z = 0$ plane since $\Omega^z(k_x,k_y,0) = -\Omega^z(k_x,k_y,0)$.

B. Symmetry condition of finite AHC

From Eq. (1), the symmetry of the Berry curvature in $\boldsymbol{k}$ space, discussed in the previous section, determines whether σ^α can be finite or not in a magnetic system. Since the Berry curvature is not affected by any translation symmetries, it is enough to take only the magnetic point group into account. If the Berry curvature satisfies the condition $\Omega^\alpha(R\boldsymbol{k}) = -\Omega^\alpha(\boldsymbol{k})$ due to a magnetic symmetry, the corresponding AHC component σ^α must be zero since the Berry curvature at $\boldsymbol{k}$ and $R\boldsymbol{k}$ are canceled out by the BZ integration [see Fig. 1(a)]. In this case, $\Omega^\alpha(\boldsymbol{k})$ is zero when R is an element of the group of $\boldsymbol{k}$, i.e., $R\boldsymbol{k} = \boldsymbol{k}$. Similarly, when a magnetic system has an n-fold rotation

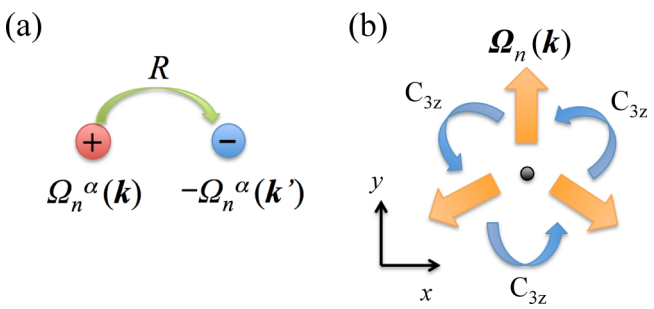

FIG. 1. Transformation of the Berry curvature under the symmetry operators. (a) Operators which reverse the sign of the Berry curvature and (b) the threefold rotation along the z axis.

TABLE II. Complete list of symmetry operators and AHC components forbidden from being finite. The translation part of the operators, which does not affect the results, is not shown. All the superscripts of the AHC are explicitly written such as $\sigma_{ij}^{\ell} \equiv \sigma^{\ell} = \sigma_{ij}$ $(i,j,\ell = x,y,z)$. $C_{n(ij)}$ indicate the n-fold rotation operators whose rotation axes are in the (ij) plane; $C_{n\mu}$ are the n-fold rotation operators along the μ axis. The mirror operator with the mirror plane normal to the μ axis is $PC_{2\mu}$. The operator $C_{n\mu}^{-1}$ belongs to the same category as that of $C_{n\mu}$ in the list. The integer in parentheses shows the number of O_h (D_{6h}) magnetic-point-group elements.

AHC component	Unitary	Antiunitary
	Cubic	
σ_{ij}^{k}	$C_{n(ij)}$, $PC_{n(ij)}$ $(n = 2,4)$ (16)	TC_{nk}, TPC_{nk} $(n = 0,2,4)$ (16)
$\sigma^{[111]}$	$C_{2[1\bar{1}0]}$, $C_{2[01\bar{1}]}$, $C_{2[\bar{1}01]}$, $PC_{2[1\bar{1}0]}$, $PC_{2[01\bar{1}]}$, $PC_{2[\bar{1}01]}$ (6)	$TC_{n[111]}$, $TPC_{n[111]}$ $(n = 0,3)$ (6)
	Hexagonal	
σ_{xy}^{z}	$C_{2(xy)}$, $PC_{2(xy)}$ (12)	TC_{nz}, TPC_{nz} $(n = 0,2,3,6)$ (12)
σ_{yz}^{x}	C_{nz}, PC_{nz} $(n = 2,3,6)$	TC_{nz}, TPC_{nz} $(n = 0,3,6)$
	C_{2y}, PC_{2y} (12)	TC_{2x}, TPC_{2x} (12)
σ_{zx}^{y}	C_{nz}, PC_{nz} $(n = 2,3,6)$	TC_{nz}, TPC_{nz} $(n = 0,3,6)$
	C_{2x}, PC_{2x} (12)	TC_{2y}, TPC_{2y} (12)

symmetry, the Berry curvature is canceled out by the BZ integration in Eq. (1) [Fig. 1(b)]. The components of $\boldsymbol{\sigma}$ normal to the n-fold axis thus disappear. For example, σ^x and σ^y are zero when the system has a rotation symmetry with respect to the z axis. We provide a complete list of the relations between the symmetry operators and the forbidden components of the AHC in Table II. The AHC component can be finite when the magnetic order breaks all of the corresponding symmetries listed in Table II. Structures of the AHC tensors under all the magnetic-point-group symmetries have been listed in Refs. [18,19] by considering the transformation coefficients for the operators of magnetic point groups. Table II is equivalent to the lists in these previous works. Note that the symmetry operators in Table II also forbid finite magnetization M_α. This is because M_α and σ^α have the same transformation property for the magnetic symmetry operations, which is a natural consequence of the same transformation property of the Berry curvature and that of the magnetic moment in $\boldsymbol{k}$ space with respect to the operators of the magnetic space group.

C. SO coupling and AHC

The effect of SO coupling on the AHE has been one of the fundamental issues since the pioneering work by Karplus and Luttinger [20]. Here, we provide a comprehensive explanation of the relation between SO coupling and the AHE in general magnetic states. First, let us note that the symmetry group for a nonmagnetic system without SO coupling is expressed as $\mathcal{M}_{\rm nmag,nso} = \mathcal{M}_{\rm para} \times SU(2)$, where $\mathcal{M}_{\rm para} = \mathcal{G} \times \{E,T\}$, $\mathcal{G}$ is the ordinary space group of the crystal structure, and E is the identity element of the space group. Magnetic order breaks both $\mathcal{M}_{\rm para}$ and $SU(2)$. However, in general, the symmetry of a magnetic system without SO coupling is higher than that with SO coupling for the following reason. The symmetry group of a magnetic system without SO coupling, $\mathcal{M}_{\rm mag,nso}$, belongs to a subgroup of $\mathcal{M}_{\rm nmag,nso}$, and that with SO coupling, $\mathcal{M}_{\rm mag,so}$, belongs to a subgroup of $\mathcal{M}_{\rm para}$ because SO coupling breaks all of the symmetries related to $SU(2)$. Therefore, $\mathcal{M}_{\rm mag,so}$ is a subgroup of $\mathcal{M}_{\rm mag,nso}$. As discussed in Sec. II A, the transformation property of the Berry curvature with respect to magnetic symmetry operations is similar to that of spin in $\boldsymbol{k}$ space; that is, it is transformed as an axial vector and reversed by T. Meanwhile, the spin rotation $R_s(\theta_S,\phi_S)$ does not affect the Berry curvature in the absence of SO coupling. As a result, the magnetic symmetries listed in Table II preserved by further multiplying the spin rotations also forbid the corresponding σ^α to be finite in magnetic systems without SO coupling.

An ordinary collinear FM system is the most fundamental example in which SO coupling is required to induce the AHE. The FM systems without SO coupling always preserve the time-reversal symmetry with the spin rotations $R_S(\theta_S,\phi_S)$. The $R_S T$ symmetry preserved in the system without SO coupling was referred to as "effective T symmetry" in Ref. [31]. Coplanar AFM spin configurations also require SO coupling to induce the AHE due to the $R_S T$ symmetry preserved in the absence of SO coupling since T works as the 180° spin rotation around the axis normal to the coplanar plane [Fig. 2(a)]. If the spin moments rise up from the coplanar plane, the spin configuration after operating T cannot be brought back with the spin rotation R_S due to the spin components normal to the coplanar plane [Fig. 2(b)]. In this case, the noncoplanar spin

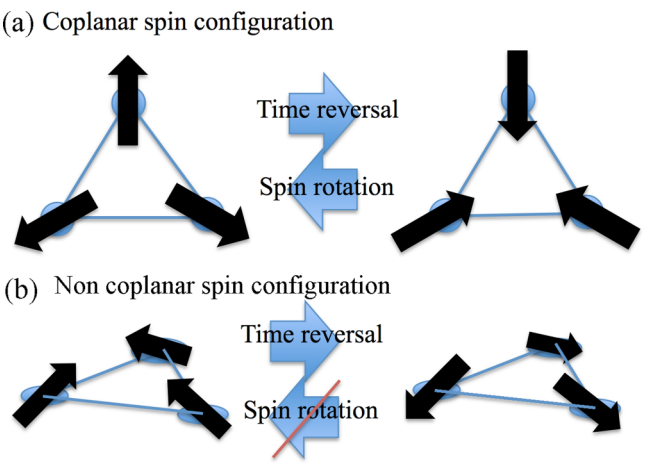

FIG. 2. Time-reversal operation and global spin rotation for (a) a coplanar spin configuration and (b) a noncoplanar spin configuration in the triangular system.

system breaks the $R_S T$ symmetry as well as T symmetry, and the AHC therefore can be finite without SO coupling. This idea also explains why scalar spin chirality can induce the AHE [6] since finite scalar spin chirality always breaks the $R_S T$ symmetry.

Mn_3Ir, Mn_3Sn, and Mn_3Ge undergo coplanar magnetic order and require SO coupling to induce the AHE from the above discussions. Indeed, the first-principles calculation for Mn_3Ir confirmed that a finite spin component normal to the coplanar plane is required for finite AHC in the absence of SO coupling [12].

III. CLUSTER MULTIPOLE MOMENTS IN AFM STATES

A. Definition of CMP

As discussed in Sec. II B, magnetic structures induce finite AHC σ^α in the same symmetry condition for finite magnetization M_α in the presence of SO coupling. This means that magnetic systems having net magnetization always belong to the symmetry which can induce the AHE with SO coupling. On the other hand, finite magnetization is not necessary to induce the AHE in AFM states. The question is then, is there a macroscopic order parameter which characterizes the AHE? To identify such an order parameter in generic magnetic states, we here introduce the cluster multipole (CMP). With the framework based on the CMP, we can quantify the symmetry breaking due to commensurate noncollinear magnetic order. Below, we provide a general theory of the CMP. A concrete example is provided in Sec. III C for Mn_3Ir and Mn_3Z.

We first identify atom clusters for which we define the CMP moments. In general, a crystal contains a number of atoms which are inequivalent under the crystal symmetry. Each atom cluster is defined as a set of atoms related to one another by the *crystal* symmetry operators without space translation in the *magnetic* unit cell. For simplicity, we here consider only the case of the magnetic order characterized by the wave vector $\boldsymbol{q} = \boldsymbol{0}$, whose magnetic unit cell is the same as that of the crystal unit cell [38]. A space group $\mathcal{G}$, which describes the symmetry of a crystal structure, is decomposed into the cosets of the maximum symmorphic subgroup $\mathcal{H}$ as

$$\mathcal{G} = \sum_{i=1}^{N_{\rm coset}} \{R_i|\boldsymbol{\tau}_i\}\mathcal{H}, \tag{5}$$

where $N_{\rm coset}$ is the number of the cosets and R_i and $\boldsymbol{\tau}_i$ represent the point-group element and translation operator of the element in space group $\mathcal{G}$, respectively, with $\{R_1|\boldsymbol{\tau}_1\} \equiv \{E|\boldsymbol{0}\}$ and $\boldsymbol{\tau}_i \neq \boldsymbol{0}$ for $i \geqslant 2$. In Eq. (5), $N_{\rm coset} = 1$ for crystal structures which belong to symmorphic space groups, and $N_{\rm coset} > 1$ for crystal structures which belong to nonsymmorphic space groups. Therefore, nonsymmorphic crystal structures contain multiple clusters related to one another by the symmetry operators $\{R_i|\boldsymbol{\tau}_i\}$ in the unit cell. The origin of the cluster is naturally defined as the point which satisfies all the point symmetries for which the cluster is defined.

Analogous to the local multipole moments defined for an atom [24,25,27], the rank-p CMP moment for the μth cluster is defined here as follows:

$$M_{pq}^{(\mu)} \equiv \sqrt{\frac{4\pi}{2p+1}} \sum_{i=1}^{N_{\rm atom}^{(\mu)}} \boldsymbol{m}_i \cdot \boldsymbol{\nabla}_i (|\boldsymbol{R}_i|^p Y_{pq}(\theta_i,\phi_i)^*), \tag{6}$$

where $N_{\rm atom}^{(\mu)}$ is the number of atoms of the μth cluster, $\boldsymbol{m}_i$ is a magnetic moment on the ith atom, $\boldsymbol{\nabla}_i \equiv \frac{\partial}{\partial \boldsymbol{R}_i}$, $\boldsymbol{R}_i \equiv (X_i, Y_i, Z_i)$ is the position of the ith atom, Y_{pq} are the spherical harmonics, and R_i, θ_i, and ϕ_i are the distance, polar angle, and azimuthal angle, respectively, of the ith atom. Based on the Wannier bases $\{w_{i,a}\}$, the magnetic moment of the ith atom is calculated as follows:

$$\boldsymbol{m}_i = \mu_B \sum_n \sum_{ab} \int \frac{d\boldsymbol{k}}{(2\pi)^3} f[\varepsilon_n(\boldsymbol{k}) - \mu] \times \langle u_n(\boldsymbol{k})|w_{i,a}\rangle \langle w_{i,a}|(\boldsymbol{\ell} + 2\boldsymbol{s})|w_{i,b}\rangle \langle w_{i,b}|u_n(\mathbf{k})\rangle, \tag{7}$$

where $\mu_B = -|e|\hbar/2m$ is the Bohr magneton and $\boldsymbol{\ell}$ and $\boldsymbol{s}$ are the orbital and spin angular momentum operators. The macroscopic contribution of the CMP moment can be defined by the summation over the clusters in the magnetic unit cell:

$$M_{pq} = \frac{N_{\rm atom}^{\rm u}}{N_{\rm atom}^{\rm c}} \frac{1}{V} \sum_{\mu=1}^{N_{\rm cluster}} M_{pq}^{(\mu)}, \tag{8}$$

where V is the volume of the magnetic unit cell, $N_{\rm atom}^{\rm u}$ is the number of atoms in the magnetic unit cell, $N_{\rm atom}^{\rm c} = \sum_\mu N_{\rm atom}^{(\mu)}$ is the total number of atoms in all of the clusters, and $N_{\rm cluster}$ is the number of clusters in the unit cell, which is the same as multiplying $N_{\rm coset}$ by the number of atoms inequivalent under the space-group symmetry.

B. Symmetry classification of CMP moments

The local multipole moments for f-electron systems are classified according to the irreducible representations (IREPs) of the point-group symmetry of the atomic site [24,26,27,39–42]. Similarly, the CMP moments can be classified according to the point-group symmetry of the atomic configuration. For a crystal structure whose conventional crystal axes are orthogonal, the CMP moments are classified according to the IREPs of the O_h point group in Table III. For a crystal structure with hexagonal conventional axes such as the hexagonal and trigonal lattice systems, the CMP moments classified according to the D_{6h} IREPs should be used to reflect the point-group symmetry. In Table IV, we provide a list of the D_{6h} CMP moments. These CMP moments are all odd with respect to the time-reversal operator T. If the magnetic structure preserves the inversion symmetry, only odd-rank CMP moments can be finite due to the relation $M_{pq} = (-)^{p+1} M_{pq}$ in Eq. (6). Figure 3 shows noncollinear magnetic structures characterized by the lowest-rank cluster octupole moments for the D_{6h} IREPs.

Ordinary magnetization M_α ($\alpha = x, y, z$) corresponds to the macroscopic contribution of the cluster dipole moment J_α. Meanwhile, magnetization of noncollinear AFM states without net dipole magnetization is characterized by the macroscopic contribution of CMP moments with ranks higher than 1. From the discussion in Sec. II B, σ^α, M_α, and J_α are transformed in the same manner as the operation of the magnetic-point-group elements, which means that they belong to the same IREPs

TABLE III. CMP moments up to rank 3 classified according to the IREPs of the O_h point group. The quadrupole CMP moments can be finite only for magnetic structures without space-inversion symmetry (see text). Note that this table is analogous to the *magnetic* multipole moments classified according to the O_h point group, and a similar list is provided for electric multipole moments in Ref. [39].

	IREP	CMP
Rank 1	T_{1g}	$J_x \equiv \frac{1}{\sqrt{2}}(-M_{11}+M_{1-1})$
(dipole)		$J_y \equiv -\frac{i}{\sqrt{2}}(M_{11}+M_{1-1})$
		$J_z \equiv M_{10}$
Rank 2	E_u	$Q_{3z^2-r^2} \equiv M_{20}$
(quadrupole)		$Q_{x^2-y^2} \equiv \frac{1}{\sqrt{2}}(M_{22}+M_{2-2})$
	T_{2u}	$Q_{yz} \equiv -\frac{i}{\sqrt{2}}(M_{21}+M_{2-1})$
		$Q_{zx} \equiv \frac{1}{\sqrt{2}}(-M_{21}+M_{2-1})$
		$Q_{xy} \equiv \frac{i}{\sqrt{2}}(M_{22}-M_{2-2})$
Rank 3	A_{2g}	$T_{xyz} \equiv \frac{i}{\sqrt{2}}(M_{32}-M_{3-2})$
(octupole)	T_{1g}	$T_x^\alpha \equiv \frac{1}{4}[\sqrt{5}(-M_{33}+M_{3-3})-\sqrt{3}(-M_{31}+M_{3-1})]$
		$T_y^\alpha \equiv \frac{i}{4}[\sqrt{5}(M_{33}+M_{3-3})+\sqrt{3}(M_{31}+M_{3-1})]$
		$T_z^\alpha \equiv M_{30}$
	T_{2g}	$T_x^\beta \equiv -\frac{1}{4}[\sqrt{3}(-M_{33}+M_{3-3})+\sqrt{5}(-M_{31}+M_{3-1})]$
		$T_y^\beta \equiv \frac{i}{4}[\sqrt{3}(M_{33}+M_{3-3})-\sqrt{5}(M_{31}+M_{3-1})]$
		$T_z^\beta \equiv \frac{1}{\sqrt{2}}(M_{32}+M_{3-2})$

of the O_h and D_{6h} point groups. The conditions for the AHE can now be concisely described with the symmetrized CMP moments. The AHE is induced by the emergence of the finite magnetization of the CMP moments which belong to the same IREP of dipole moments, i.e., T_{1g} (A_{2g} and/or E_{1g}) CMP moments in the O_h (D_{6h}) representation. Note that, in the absence of SO coupling, the AHE requires R_sT-symmetry breaking as well as magnetization of these CMP moments, as discussed in Sec. II C.

TABLE IV. CMP moments up to rank 3 classified according to the IREPs of the D_{6h} point group. Note that this table is analogous to the *magnetic* multipole moments classified according to the D_{6h} point group. The quadrupole CMP moments can be finite only for magnetic structures without space-inversion symmetry (see text).

	IREP	CMP
Rank 1	A_{2g}	$J_z \equiv M_{10}$
(dipole)	E_{1g}	$J_x \equiv \frac{1}{\sqrt{2}}(-M_{11}+M_{1-1})$
		$J_y \equiv -\frac{i}{\sqrt{2}}(M_{11}+M_{1-1})$
Rank 2	A_{1u}	$Q_{3z^2-r^2} \equiv M_{20}$
(quadrupole)	E_{2u}	$Q_{x^2-y^2} \equiv \frac{1}{\sqrt{2}}(M_{22}+M_{2-2})$
		$Q_{xy} \equiv \frac{i}{\sqrt{2}}(M_{22}-M_{2-2})$
	E_{1u}	$Q_{zx} \equiv \frac{1}{\sqrt{2}}(-M_{21}+M_{2-1})$
		$Q_{yz} \equiv -\frac{i}{\sqrt{2}}(M_{21}+M_{2-1})$
Rank 3	A_{2g}	$T_z^\alpha \equiv M_{30}$
(octupole)	E_{1g}	$T_x^\gamma \equiv \frac{1}{\sqrt{2}}(-M_{31}+M_{3-1})$
		$T_y^\gamma \equiv -\frac{i}{\sqrt{2}}(M_{31}+M_{3-1})$
	E_{2g}	$T_{xyz} \equiv \frac{i}{\sqrt{2}}(M_{32}-M_{3-2})$
		$T_z^\beta \equiv \frac{1}{\sqrt{2}}(M_{32}+M_{3-2})$
	B_{2g}	$T_x^\zeta \equiv \frac{1}{\sqrt{2}}(-M_{33}+M_{3-3})$
	B_{1g}	$T_y^\zeta \equiv \frac{i}{\sqrt{2}}(M_{33}+M_{3-3})$

C. CMP moment and AHE in Mn_3Ir and Mn_3Z

Let us now apply the scheme discussed above to the AFM spin configurations observed in Mn_3Ir and Mn_3Z, for which the AHE in the AFM states has been studied [12,14–16]. Mn_3Ir crystallizes into the simple cubic structure which belongs to the space group $Pm\bar{3}m$ (O_h^1, space group 221), as shown in Fig. 4. This crystal structure leads to $N_{\rm coset} = 1$ in Eq. (5) since the space group is symmorphic. Here, we focus on the Mn atoms, which have finite magnetic moments in the AFM state. The unit cell contains three Mn atoms ($N^u_{\rm atom} = 3$), and we can define a Mn cluster, which contains six Mn atoms ($N^c_{\rm atom} = 6$) related to each other by the operation of the symmetry elements of the O_h point group. In Fig. 4(b), we show the AFM structures

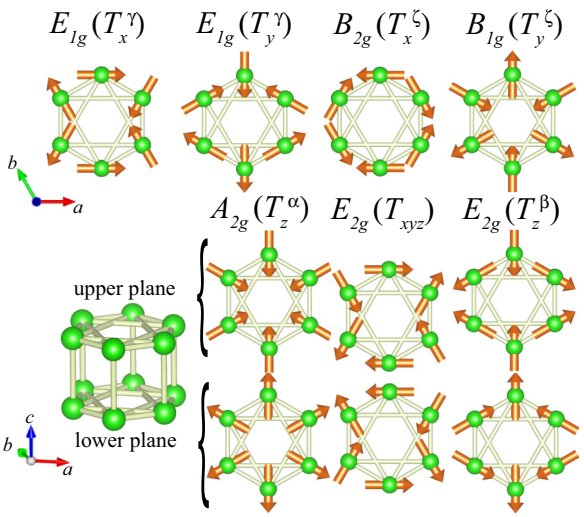

FIG. 3. AFM structures characterized by the cluster octupole moments of the D_{6h} IREPs in Table IV.

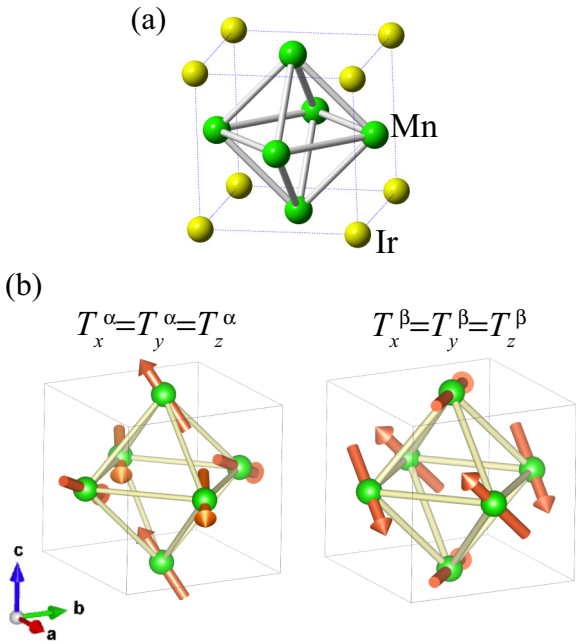

FIG. 4. (a) Crystal structure of Mn_3Ir. (b) The AFM structures characterized by the cluster octupole moments of T_{1g} CMP with the relation $T_x^\alpha = T_y^\alpha = T_z^\alpha$, which has been recognized experimentally, and of T_{2g} CMP with $T_x^\beta = T_y^\beta = T_z^\beta$ in the Mn cluster of Mn_3Ir.

characterized by the T_{1g} octupole moment with the order parameter $T_x^\alpha = T_y^\alpha = T_z^\alpha$, which has been recognized experimentally, and the T_{2g} octupole moment with $T_x^\beta = T_y^\beta = T_z^\beta$. Following the discussion in Sec. III B, the AFM configuration with T_{1g} cluster octupole moments, which belong to the same IREP as the dipole moment, can induce the AHE, as predicted in the earlier work using first-principles calculations [12], while that with T_{2g} does not. The magnetic symmetries broken by the T_{1g} cluster octupole moment are completely the same as those broken by the colinear magnetic dipole order along the [111] direction. As a result, the magnetic space group ($R\bar{3}m'$) for the AFM state with the T_{1g} CMP, whose symmetry elements are listed in Table V, is the same as that for the FM state.

Mn_3Z crystallizes into the Ni_3Sn-type structure, as shown in Fig. 5(a). The hexagonal structure of Mn_3Z belongs to the

TABLE V. Magnetic symmetry operators preserved in the AFM states of Mn_3Ir and Mn_3Sn. In Mn_3Ir, the directions of the rotation axes are expressed with the cubic (Cartesian) axis. In Mn_3Sn, the x and y axes are shown in Fig. 5(b), and the z axis is the normal direction of the xy plane. $\boldsymbol{\tau}$ represents the translation $(0,0,c/2)$.

Spin structure	Preserved symmetries
Mn_3Ir	$\{E \mid \mathbf{0}\},\{C^+_{3[111]} \mid \mathbf{0}\},\{C^-_{3[111]} \mid \mathbf{0}\},$ $T\{C_{2[1\bar{1}0]} \mid \mathbf{0}\},T\{C_{2[01\bar{1}]} \mid \mathbf{0}\},T\{C_{2[\bar{1}01]} \mid \mathbf{0}\}$ $\{P \mid \mathbf{0}\},\{PC^+_{3[111]} \mid \mathbf{0}\},\{PC^-_{3[111]} \mid \mathbf{0}\},$ $T\{PC_{2[1\bar{1}0]} \mid \mathbf{0}\},T\{PC_{2[01\bar{1}]} \mid \mathbf{0}\},T\{PC_{2[\bar{1}01]} \mid \mathbf{0}\}$
Mn_3Sn AFM1	$\{E \mid \mathbf{0}\},\{C_{2x} \mid \mathbf{0}\},T\{C_{2z} \mid \boldsymbol{\tau}\},T\{C_{2y} \mid \boldsymbol{\tau}\},$ $\{P \mid \mathbf{0}\},\{PC_{2x} \mid \mathbf{0}\},T\{PC_{2z} \mid \boldsymbol{\tau}\},T\{PC_{2y} \mid \boldsymbol{\tau}\}$
Mn_3Sn AFM2	$\{E \mid \mathbf{0}\},\{C_{2y} \mid \boldsymbol{\tau}\},T\{C_{2z} \mid \boldsymbol{\tau}\},T\{C_{2x} \mid \mathbf{0}\},$ $\{P \mid \mathbf{0}\},\{PC_{2y} \mid \boldsymbol{\tau}\},T\{PC_{2z} \mid \boldsymbol{\tau}\},T\{PC_{2x} \mid \mathbf{0}\}$

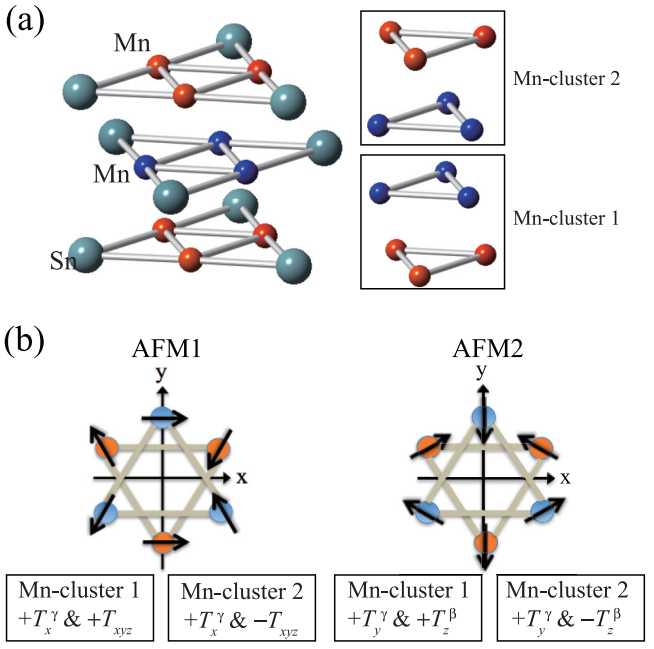

FIG. 5. (a) Crystal structure of Mn_3Z (Z = Sn, Ge) with the Mn clusters defined by the space group (see text). (b) Spin configuration of the Mn atoms in Mn_3Sn. The AFM1 and AFM2 spin structures are experimentally realized depending on the direction of magnetic fields along the x and y directions, respectively [45]. The lowest-rank CMP moments characterizing the spin configurations are also shown for each Mn cluster.

space group $P6_3/mmc$ (D^4_{6h}, space group 194) [43,44]. The nonsymmorphic space group $P6_3/mmc$ is decomposed into the cosets of the symmorphic space group $P\bar{3}m1$ (D^3_{3d}, space group 164) as $P6_3/mmc = P\bar{3}m1 + \{C_{2z}|\boldsymbol{\tau}\}P\bar{3}m1$ ($D^3_{3d} + \{C_{2z}|\boldsymbol{\tau}\}D^3_{3d}$), where $\boldsymbol{\tau} = (0,0,c/2)$. Following the discussion in Sec. III, Mn_3Z contains four clusters, i.e., two clusters related to each other by the operation of $\{C_{2z}|\boldsymbol{\tau}\}$ for Mn and Z atoms in the magnetic unit cell [see Fig. 5(a)]. Each cluster has the point-group symmetry of D_{3d}. Since the magnetic moments in Z atoms are negligible, we here ignore the Z-atom clusters. The macroscopic contribution of the CMP moment is calculated from Eq. (8) with $N^{\rm u}_{\rm atom}/N^{\rm c}_{\rm atom} = 1/2$ since the unit cell of Mn_3Z contains six Mn atoms ($N^{\rm u}_{\rm atom} = 6$) and two Mn clusters consist of six Mn atoms in each cluster ($N^{\rm c}_{\rm atom} = 12$), as shown in Fig. 5(a). The D_{3d} point group has six IREPs, $A'_{1g/u}$, $A'_{2g/u}$, $E'_{g/u}$, in which the prime distinguishes the IREPs from those of the D_{6h} point group. The compatibility relations between the D_{3d} and D_{6h} IREPs are as follows:

$$A_{1g/u}\downarrow D_{3d} = B_{2g/u}\downarrow D_{3d} = A'_{1g/u},$$
$$A_{2g/u}\downarrow D_{3d} = B_{1g/u}\downarrow D_{3d} = A'_{2g/u},$$
$$E_{1g/u}\downarrow D_{3d} = E_{2g/u}\downarrow D_{3d} = E'_{g/u}.$$

These relations mean, for instance, the A_{1g} and B_{2g} CMP moments belong to the same IREP, A'_{1g}, in the cluster with the D_{3d} point-group symmetry.

Next, we identify the CMP moments which characterize the AFM states of Mn_3Z. We mainly focus on the AFM states of

Mn_3Sn, whose magnetic structures have been well established experimentally [44–46]. Mn magnetic moments in Mn_3Sn form the so-called inverse triangular spin structure below the Néel temperature of $T_{N1} \simeq 420$ K [44,45] [Fig. 5(b)]. Mn_3Sn undergoes another phase transition at $T_{N2} \sim 50$ K, but the detailed magnetic structure for the low-temperature phase is unknown. We therefore focus on the magnetic phase above 50 K. Interestingly, the inverse triangular spin structure rotates following the direction of applied magnetic fields in the c plane [46]. We refer to the magnetic structures under the magnetic fields along the x and y directions as AFM1 and AFM2, respectively, as shown in Fig. 5(b). The magnetic space groups of the AFM1 and AFM2 magnetic structures belong to $Cmc'm'$ and $Cm'cm'$, respectively, taking the primary, secondary, and tertiary directions as the x, y, and z axes. The symmetry operators in the magnetic space group are listed in Table V. The magnetic space groups of the AFM1 and AFM2 states are the same as those of the FM states with the magnetic moments along the x and y directions, respectively. Furthermore, these AFM states require SO coupling, like FM states, to induce the AHE from the discussion in Sec. II C on the coplanar spin configuration.

Because of the geometry of the magnetic alignments on the Mn atoms, there is no magnetization of the dipole moment if all the atoms have the same size of local magnetic moment [47]. Also, since the magnetic structures preserve the inversion symmetry, only the odd-rank CMP moments are finite. Indeed, the CMP moments calculated for the AFM states with Eq. (6) are finite only for odd ranks higher than 1. The lowest-rank CMP moments characterizing the AFM spin configurations are thus cluster octupole moments.

For the symmetry operators in the D_{3d} point group, the AFM1 (AFM2) magnetic configuration of Mn_3Sn has the same transformation property as the magnetic structure characterized by T_x^γ and T_{xyz} (T_y^γ and T_z^β) in Fig. 3. Namely, the magnetic modulation of AFM1 (AFM2) parallel to the xy plane is characterized by T_x^γ (T_y^γ), and the three-dimensional configuration is characterized by T_{xyz} (T_z^β). The magnetic configurations in the different clusters are related to each other by the operation of TC_{2z} (see Table V and Fig. 5). The operation of TC_{2z} preserves T_x^γ (T_y^γ) and flips the sign of T_{xyz} (T_z^β) due to the transformation property of each IREP. As a result, T_x^γ and T_{xyz} (T_y^γ and T_z^β) octupole moments have ferromagnetic and antiferromagnetic alignments, respectively, between the neighboring clusters. Therefore, only the T_x^γ (T_y^γ) octupole moment can have macroscopic magnetization in the AFM1 (AFM2) state.

In Fig. 6, we show how the cluster octupole moments in Mn_3Sn and Mn_3Ge change as a function of the local magnetic moment [48]. Here, we assumed that all the Mn sites always have the same size of local magnetic moment and Mn_3Ge has the same spin configurations as those of Mn_3Sn. In this situation, we can show from Eq. (6) that the octupole moments are proportional to the local magnetic moments. Thus, the local moment can also quantify the symmetry breaking associated with the AHE. The local magnetic moment, however, cannot characterize general AFM orders when inequivalent magnetic atoms have different sizes of local moments. On the other hand, even in such cases, the CMP moments work as the order parameter quantifying the symmetry breaking.

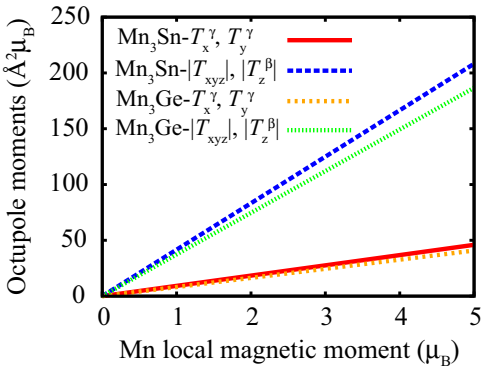

FIG. 6. Local magnetic moment dependence of the cluster octupole moments for the Mn clusters in Mn_3Sn and Mn_3Ge. The parameters for the crystal structures are described in Sec. IV A. T_x^γ and T_{xyz} (T_y^γ and T_z^β) are for AFM1 (AFM2) in Fig. 5.

IV. FIRST-PRINCIPLES ANALYSIS OF ANOMALOUS HALL EFFECT

A. Method

We performed the first-principles calculations for the AFM1 and AFM2 states of Mn_3Z (Z = Sn, Ge) with the QUANTUM ESPRESSO package [49] with the relativistic version of the ultrasoft pseudopotentials using the exchange-correlation functional of the generalized gradient approximation (GGA) proposed by Perdew, Burke, and Ernzerhof [50]. We used the lattice constants $a = 5.665$ Å, $c = 4.531$ Å and the Wyckoff position of the Mn $6h$ atomic sites $x = 0.8388$ from the experimental results [43,44]. For Mn_3Ge, the lattice constants $a = 5.34$ Å, $c = 4.31$ Å from the experiment were adopted [15], and the Wyckoff parameter of the Mn $6h$ atomic sites was taken to be the same as that of Mn_3Sn. The spin configuration was set as in Fig. 5(b) for the AFM1 and AFM2 spin configurations. In the GGA calculations, we obtained the local magnetic moment $3.39\mu_B$ for Mn_3Sn and $2.92\mu_B$ for Mn_3Ge for both the AFM1 and AFM2 states. The calculations were performed also for bcc Fe as a reference FM system. The lattice constant 2.87 Å was used. The spin moment was set to the $+z$ direction. The magnetic moment obtained from the GGA calculation is $2.22\mu_B$.

The realistic tight-binding models were obtained from the first-principles band structures using the WANNIER90 program code [51]. The tight-binding model for bcc Fe was generated with 18 orbitals Fe s, p, and d orbitals, and that for Mn_3Z was generated with 88 orbitals using Mn s, d and Z s, p orbitals. The energy band structures of the tight-binding models show good agreement with those of the first-principles calculations, as shown in Fig. 7. The Berry curvature and AHC were calculated within the tight-binding models with Eqs. (1), (2), and (3).

To discuss the magnetic-moment dependence of the AHC, we also performed the calculations for nonmagnetic states with SO coupling and obtained the tight-binding Hamiltonian $H_{\rm nmag}$ as well as the Hamiltonian for the magnetic state with SO coupling $H_{\rm mag}$. We further generated the hopping matrices obtained by interpolating or extrapolating these tight-binding Hamiltonian matrices as $H_\lambda = H_{\rm nmag} + \lambda(H_{\rm mag} - H_{\rm nmag})$ ($\lambda \geqslant 0$). The Fermi level was determined to preserve

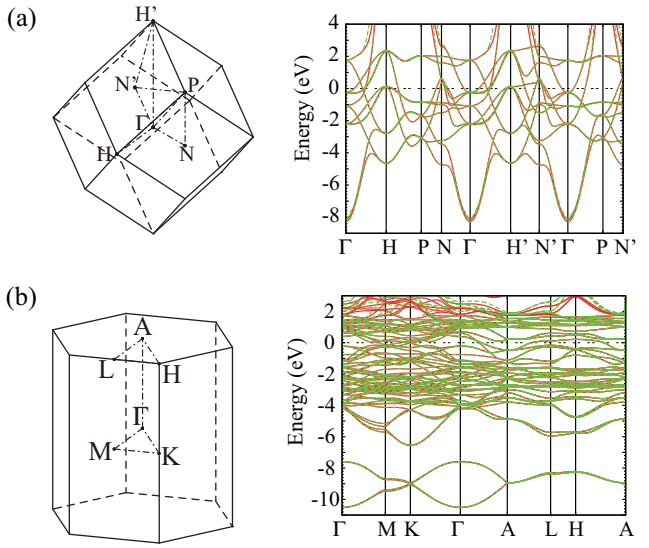

FIG. 7. BZ and the energy bands for (a) the FM state of bcc Fe and (b) the AFM1 state of Mn_3Sn. The red and green lines are the energy bands obtained from the first-principles calculations and from the Wannier interpolation, respectively.

the electron number for each H_λ, and then the AHC was calculated for the obtained electronic structure and the Fermi level.

B. Ferromagnetic states of bcc Fe

Before proceeding to the first-principles analysis of the AFM states of Mn_3Z, we discuss the AHE in the FM states of bcc Fe, which has been well investigated theoretically [30–32,52]. Figure 8 shows the magnetic moment (cluster dipole moment) dependence of the AHC for bcc Fe. The AHC increases as the magnetic moment increases in the small magnetic-moment region and makes a peak around $2.22\mu_B$, obtained in the GGA calculation, and then decreases. Figures 9(a) and 9(b) show the spin density of states (DOS) of the Fe d orbitals for the electronic structures with magnetic moments $2.22\mu_B$ and $2.86\mu_B$, respectively. The original

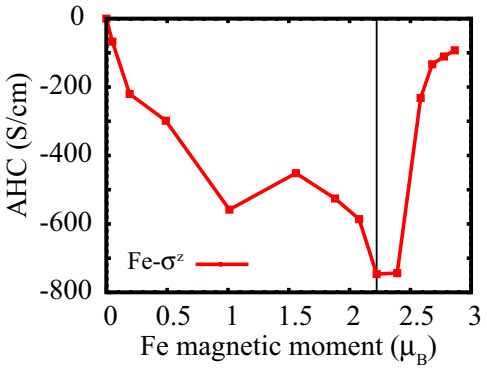

FIG. 8. Local magnetic moment (cluster dipole moment) dependence of the AHC in the FM states of bcc Fe. The solid line indicates the local magnetic moment obtained by the first-principles calculation.

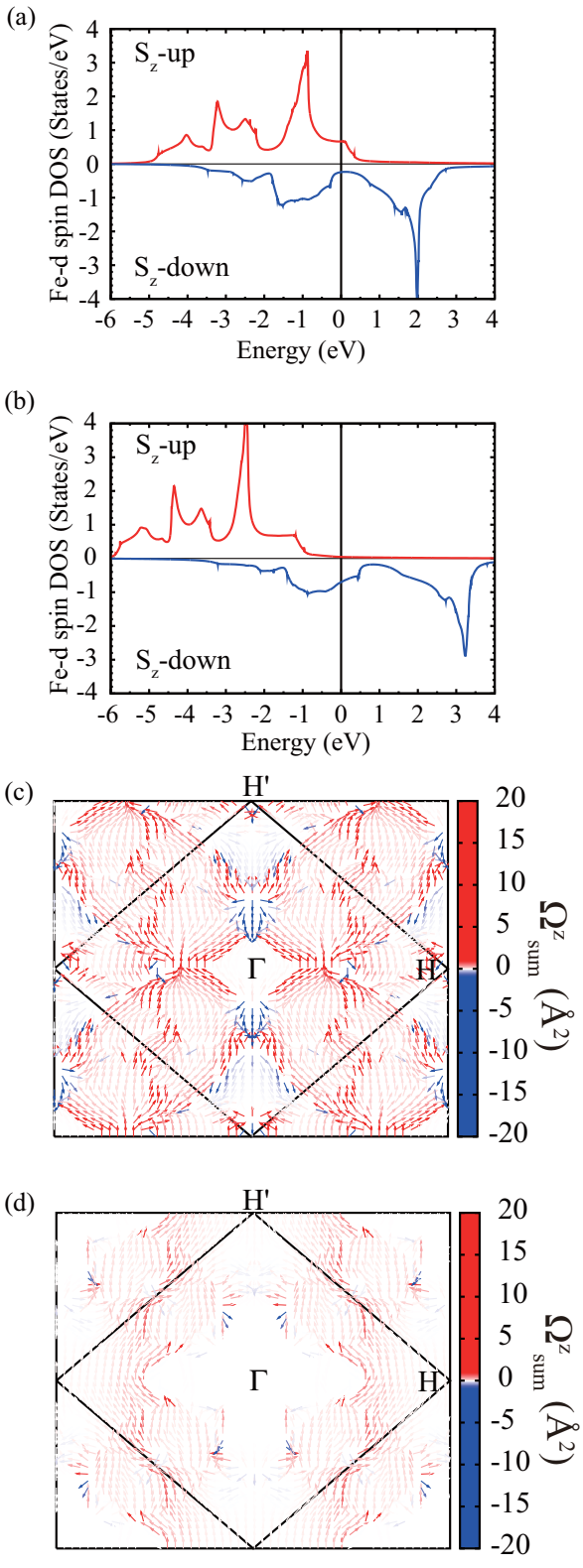

FIG. 9. Fe d spin-projected DOS for the FM states of bcc Fe with the magnetic moments (a) $2.22\mu_B$ and (b) $2.86\mu_B$ corresponding to $\lambda = 1.0$ and 2.0, respectively. (c) and (d) $\Omega_{\rm sum}(\boldsymbol{k})$ (see text) on the $k_y = 0$ plane corresponding to the states in (a) and (b), respectively. $\Omega_{\rm sum}$ vectors are colored by the weight of $\Omega^z_{\rm sum}$, which contributes to the AHC.

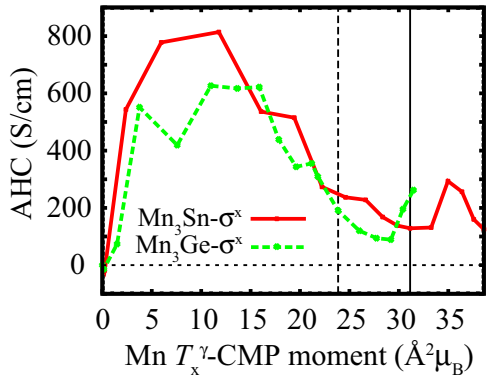

FIG. 10. Mn cluster T_x^γ octupole moment dependence of the AHC in AFM1 states of Mn_3Sn and Mn_3Ge. The solid and dashed lines indicate the local magnetic moments obtained with the first-principles calculations for Mn_3Sn and Mn_3Ge, respectively.

magnetic state with the magnetic moment $2.22\mu_B$ has contributions from both the majority- (up-) and minority- (down-) spin DOSs at the Fermi level. Meanwhile, the DOS in Fig. 9(b) shows that the spin-up states are almost fully occupied due to the large spin moment and do not have weight at the Fermi level. Figures 9(c) and 9(d) show the $\boldsymbol{k}$ dependence of the Berry curvature summed over the occupied states, $\Omega_{\rm sum}(\boldsymbol{k}) = \sum_n f[\varepsilon_n(\boldsymbol{k}) - \mu]\Omega_n(\boldsymbol{k})$, on the $k_y = 0$ plane. In both states, $\Omega^z_{\rm sum}$ is positive in a large region of the BZ, leading to negative σ^z via the BZ integration. Meanwhile, we see that the intensity of $\Omega^z_{\rm sum}(\boldsymbol{k})$ is much stronger in Fig. 9(c) than in Fig. 9(d).

C. Antiferromagnetic states of Mn_3Sn

Let us move on to Mn_3Z. Here, we mainly focus on the AFM1 state of Mn_3Sn, whose crystal and magnetic structures have been well established experimentally [44–46]. The local Mn magnetic moment $3.39\mu_B$ and $\sigma_{yz} = 129$ S/cm obtained from the GGA calculation agree well with the experimental measurement of the local magnetic moment $3\mu_B$ and that of the AHC ~ 100 S/cm [14]. The calculated value is also consistent with a recent study [23]. Figure 10 shows that the AHC in Mn_3Sn and Mn_3Ge shows a similar CMP moment dependence. The calculations also show that decreasing the magnetic moments from the one obtained with GGA makes the size of the AHC larger. In fact, for the electronic structure obtained with the GGA calculation, the AHC (magnetization) of Mn_3Ge is larger (smaller) than that of Mn_3Sn. This is consistent with the recent experiments [14–16].

For the AFM states of Mn_3Sn, we define the Mn cluster spin bases as the two symmetrized spin configurations related by the time-reversal symmetry [see the insets in Figs. 11(a) and 11(b)]. The two spin configurations are characterized by the positive and negative T_x^γ octupole moments. Then, we can discuss the AHE in terms of the spin cluster, in analogy with the majority- and minority-spin states in the FM systems. Figures 11(a) and 11(b) show the projected DOS for each spin cluster corresponding to $T_x^\gamma = 11.8$ Å$^2\mu_B$ and 31.2 Å$^2\mu_B$, respectively. The magnetic state with $T_x^\gamma = 11.8$ Å$^2\mu_B$ has a large DOS contribution from both spin cluster components at

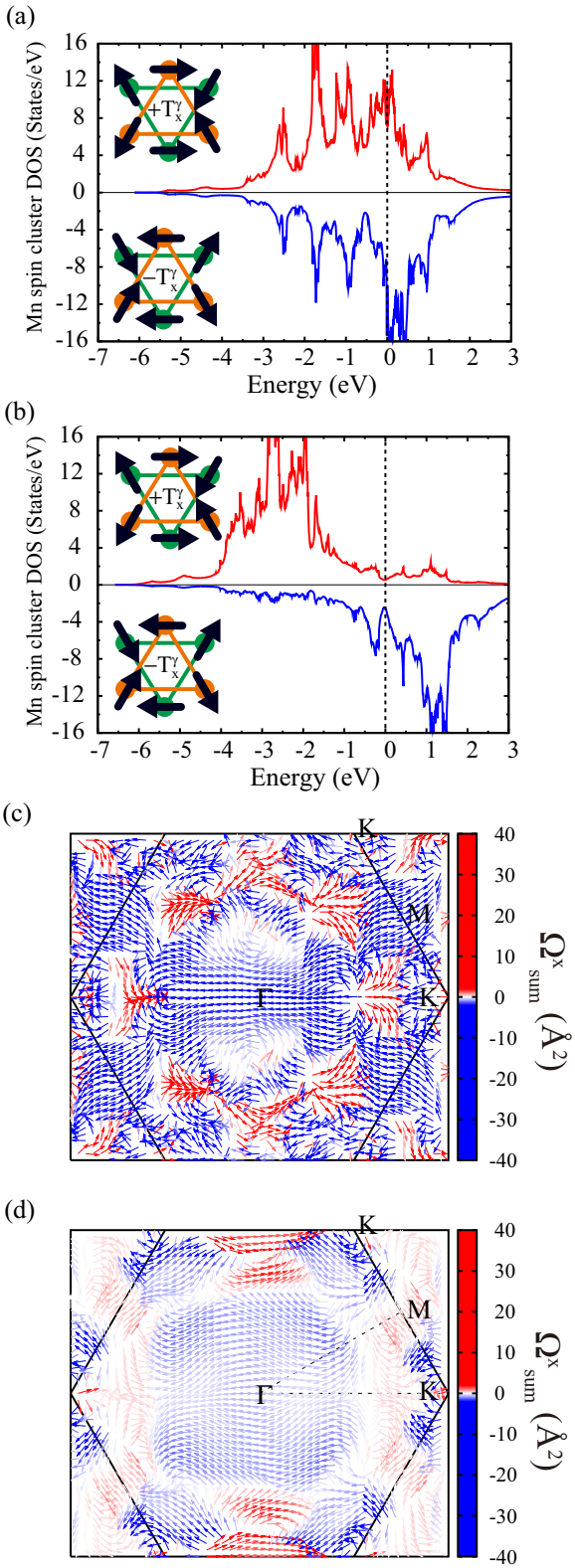

FIG. 11. Projected DOS for the AFM states of Mn_3Sn with the Mn T_x^γ CMP (local magnetic moment): (a) 11.8 Å$^2\mu_B$ ($1.28\mu_B$) and (b) 31.2 Å$^2\mu_B$ ($3.39\mu_B$), corresponding to $\lambda = 0.20$ and 1.0, respectively. (c) and (d) $\Omega_{\rm sum}(\boldsymbol{k})$ (see text) on the $k_z = 0$ plane corresponding to the states in (a) and (b), respectively. $\Omega_{\rm sum}$ vectors are colored by the weight of $\Omega^x_{\rm sum}$, which contributes to the AHC.

the Fermi level. On the other hand, in the magnetic state with the large T_x^γ moment, the spin-cluster states characterized by the positive T_x^γ are almost fully occupied due to the large octupole moment and have only small weight at the Fermi level. Figures 11(c) and 11(d) show $\Omega_{\rm sum}(\boldsymbol{k})$ colored by the $\Omega^x_{\rm sum}$ component on the $k_z = 0$ plane. In both states, $\Omega^x_{\rm sum}$ is negative in a large region of the BZ, leading to positive σ^x via the BZ integration. The intensity of $\Omega^x_{\rm sum}(\boldsymbol{k})$ is stronger in Fig. 11(c) than in Fig. 11(d), which is a situation similar to that in Figs. 9(c) and 9(d).

V. SUMMARY

We showed that the symmetry breaking due to the commensurate noncollinear magnetic order can be measured with the CMP moment, which is defined for atomic clusters in the crystal. We identified the degree of freedom responsible for the AHE in generic magnetic systems as the macroscopic contribution of T_{1g} (A_{2g} and/or E_{1g}) CMP moments for the O_h (D_{6h}) point-group representation. The theoretical framework was applied to the AFM states of Mn_3Ir and Mn_3Z. The AFM1 (AFM2) state of Mn_3Sn is characterized by the T_x^γ and T_{xyz} (T_y^γ and T_z^β) cluster octupole moments in the D_{6h} IREPs, and the AHE is induced by the macroscopic contribution of T_x^γ (T_y^γ) with SO coupling. The AHC in the FM states of bcc Fe and that in the AFM states of Mn_3Sn show similar dependence on the CMP moments. Thus, the CMP makes it possible to discuss the FM and AFM states in the same framework and is useful to search for another new functional material with a large AHE.

ACKNOWLEDGMENTS

We thank S. Nakatsuji, H. Kusunose, and T. Miyake for helpful comments and discussions. This work was supported by JSPS KAKENHI Grants No. JP15K17713, No. JP15H05883 (J-Physics), No. JP16H04021, No. JP16H00924, and No. JP16H06345 and PRESTO and CREST, Japan Science and Technology Agency.

[1] N. Nagaosa, J. Sinova, S. Onoda, A. MacDonald, and N. Ong, Rev. Mod. Phys. **82**, 1539 (2010).
[2] D. Xiao, M.-C. Chang, and Q. Niu, Rev. Mod. Phys. **82**, 1959 (2010).
[3] M. Gradhand, D. V. Fedorov, F. Pientka, P. Zahn, I. Mertig, and B. L. Gyrffy, J. Phys. Condens. Matter **24**, 213202 (2012).
[4] S. Yoshii, S. Iikubo, T. Kageyama, K. Oda, Y. Kondo, K. Murata, and M. Sato, J. Phys. Soc. Jpn. **69**, 3777 (2000).
[5] Y. Taguchi, Y. Oohara, H. Yochizawa, N. Nagaosa, and Y. Tokura, Science **291**, 2573 (2001).
[6] R. Shindou and N. Nagaosa, Phys. Rev. Lett. **87**, 116801 (2001).
[7] Y. Yasui, T. Kageyama, T. Moyoshi, M. Soda, M. Sato, and K. Kakurai, J. Phys. Soc. Jpn. **75**, 084711 (2006).
[8] T. Tomizawa and H. Kontani, Phys. Rev. B **80**, 100401 (2009).
[9] T. Tomizawa and H. Kontani, Phys. Rev. B **82**, 104412 (2010).
[10] Y. Taguchi, T. Sasaki, S. Awaji, Y. Iwasa, T. Tayama, T. Sakakibara, S. Iguchi, T. Ito, and Y. Tokura, Phys. Rev. Lett. **90**, 257202 (2003).
[11] Y. Taguchi, Y. Oohara, H. Yoshizawa, N. Nagaosa, T. Sasaki, S. Awaji, Y. Iwasa, T. Tayama, T. Sakakibara, S. Iguchi *et al.*, J. Phys. Condens. Matter **16**, S599 (2004).
[12] H. Chen, Q. Niu, and A. H. MacDonald, Phys. Rev. Lett. **112**, 017205 (2014).
[13] J. Kübler and C. Felser, Europhys. Lett. **108**, 67001 (2014).
[14] S. Nakatsuji, N. Kiyohara, and T. Higo, Nature (London) **527**, 212 (2015).
[15] N. Kiyohara, T. Tomita, and S. Nakatsuji, Phys. Rev. Appl. **5**, 064009 (2016).
[16] A. K. Nayak, J. E. Fischer, Y. Sun, B. Yan, J. Karel, A. C. Komarek, C. Shekhar, N. Kumar, W. Schnelle, J. Kübler *et al.*, Sci. Adv. **2**, e1501870 (2016).
[17] H. Yang, Y. Sun, Y. Zhang, W.-J. Shi, S. S. P. Parkin, and B. Yan, New J. Phys. **19**, 015008 (2017).
[18] W. Kleiner, Phys. Rev. **142**, 318 (1966).
[19] M. Seemann, D. Ködderitzsch, S. Wimmer, and H. Ebert, Phys. Rev. B **92**, 155138 (2015).
[20] R. Karplus and J. Luttinger, Phys. Rev. **95**, 1154 (1954).
[21] It has been proposed that the scalar spin chirality can induce the AHE also in the spin liquid state. See, e.g., Y. Machida, S. Nakatsuji, S. Onoda, T. Tayama, and T. Sakakibara, Nature (London) **463**, 210 (2010).
[22] N. Nagaosa and Y. Tokura, Nat. Nanotechnol. **8**, 899 (2013).
[23] Y. Zhang, Y. Sun, H. Yang, J. Železný, S. S. P. Parkin, C. Felser, and B. Yan, Phys. Rev. B **95**, 075128 (2017).
[24] H. Kusunose, J. Phys. Soc. Jpn. **77**, 064710 (2008).
[25] Y. Kuramoto, Prog. Theor. Phys. Suppl. **176**, 77 (2008).
[26] Y. Kuramoto, H. Kusunose, and A. Kiss, J. Phys. Soc. Jpn. **78**, 072001 (2009).
[27] P. Santini, S. Carretta, G. Amoretti, R. Caciuffo, N. Magnani, and G. H. Lander, Rev. Mod. Phys. **81**, 807 (2009).
[28] M.-T. Suzuki, N. Magnani, and P. M. Oppeneer, Phys. Rev. B **82**, 241103 (2010).
[29] M.-T. Suzuki, N. Magnani, and P. M. Oppeneer, Phys. Rev. B **88**, 195146 (2013).
[30] X. Wang, J. R. Yates, I. Souza, and D. Vanderbilt, Phys. Rev. B **74**, 195118 (2006).
[31] D. Gosálbez-Martínez, I. Souza, and D. Vanderbilt, Phys. Rev. B **92**, 085138 (2015).
[32] Z. Fang, N. Nagaosa, K. S. Takahashi, A. Asamitsu, R. Mathieu, T. Ogasawara, H. Yamada, M. Kawasaki, Y. Tokura, and K. Terakura, Science **302**, 92 (2003).
[33] M. Onoda and N. Nagaosa, J. Phys. Soc. Jpn. **71**, 19 (2002).
[34] T. Jungwirth, Q. Niu, and A. H. MacDonald, Phys. Rev. Lett. **88**, 207208 (2002).
[35] D. J. Thouless, M. Kohmoto, M. P. Nightingale, and M. den Nijs, Phys. Rev. Lett. **49**, 405 (1982).
[36] M.-C. Chang and Q. Niu, Phys. Rev. B **53**, 7010 (1996).
[37] G. Sundaram and Q. Niu, Phys. Rev. B **59**, 14915 (1999).
[38] Generalization of the definition for commensurate magnetic order with $\boldsymbol{q} \neq 0$ is straightforward by considering the magnetic unit cell expanded from the crystal unit cell.

[39] R. Shiina, H. Shiba, and P. Thalmeier, J. Phys. Soc. Jpn. **66**, 1741 (1997).
[40] A. Kiss and P. Fazekas, Phys. Rev. B **71**, 054415 (2005).
[41] T. Takimoto, J. Phys. Soc. Jpn. **75**, 034714 (2006).
[42] M.-T. Suzuki and H. Ikeda, Phys. Rev. B **90**, 184407 (2014).
[43] S. Tomiyoshi, J. Phys. Soc. Jpn. **51**, 803 (1982).
[44] P. Brown, V. Nunez, F. Tasset, J. Forsyth, and P. Radhakrishna, J. Phys. Condens. Matter **2**, 9409 (1990).
[45] S. Tomiyoshi and Y. Yamaguchi, J. Phys. Soc. Jpn. **51**, 2478 (1982).
[46] T. Nagamiya, S. Tomiyoshi, and Y. Yamaguchi, Solid State Commun. **42**, 385 (1982).
[47] Experiments observe a tiny net magnetization $M \sim 0.002\mu_B$, most likely due to the deviation of the magnetic structure.
[48] We consider only the contribution of the spin moments for the CMPs in Eqs. (6) and (7) since the orbital moments are negligible due to the small SO coupling in the 3*d* electron systems.
[49] P. Giannozzi, S. Baroni, N. Bonini, M. Calandra, R. Car, C. Cavazzoni, D. Ceresoli, G. L. Chiarotti, M. Cococcioni, I. Dabo *et al.*, J. Phys. Condens. Matter **21**, 395502 (2009).
[50] J. P. Perdew, K. Burke, and M. Ernzerhof, Phys. Rev. Lett. **77**, 3865 (1996).
[51] A. A. Mostofi, J. R. Yates, Y.-S. Lee, I. Souza, D. Vanderbilt, and N. Marzari, Comput. Phys. Commun. **178**, 685 (2008).
[52] Y. Yao, L. Kleinman, A. H. MacDonald, J. Sinova, T. Jungwirth, D.-s. Wang, E. Wang, and Q. Niu, Phys. Rev. Lett. **92**, 037204 (2004).